Proceedings M2D2022 - 9th International Conference on Mechanics and Materials in Design
Funchal/Portugal 26-30 June 2022, Editors J.F. Silva Gomes and S.A. Meguid, pp.1035-1050
https://paginas.fe.up.pt/~m2d/proceedings_m2d2022/

PAPER REF: 19120

COMPUTATIONAL FLUID DYNAMICS OF THE LUBRICANT FLOW IN THE SEALING GAP OF ROTARY SHAFT SEALS

Jeremias Grün(*), Simon Feldmeth, Frank Bauer
University of Stuttgart - Institute of Machine Components, Germany
(*)*Email:* jeremias.gruen@ima.uni-stuttgart.de

ABSTRACT

The lubricant flow in the sealing gap significantly affects the sealing behavior of rotary shaft seals. Computational fluid dynamics (CFD) are applied here to analyze these fluid flows. A decisive input parameter is the sealing gap height respectively the lubricant film thickness. The film thickness is estimated on the basis of several analytical elastohydrodynamic lubrication (EHL) equations. The results for sealing characteristics such as the pumping rate and the friction torque derived from the numerical analyses are compared and discussed with the results obtained from test rig studies. This allows the validity of the applied methods to be verified.

Keywords: tribology, rotary shaft seals, computational fluid dynamics (CFD), elastohydrodynamic lubrication (EHL), film thickness prediction.

INTRODUCTION

Rotary shaft seals have been used for decades to seal shaft passages on a wide variety of industrial aggregates. The complex tribological system rotary shaft seal shown in Figure 1 involves the sealing ring itself, the sealing counterface (shaft) and the fluid to be sealed (lubricant). Under operation, the sealing gap filled with lubricant builds up in the contact area between the sealing edge and the shaft. An overview of the fundamentals of tribology and the function of rotary shaft seals can be found in (Bauer, 2021b, 2021a). The modeling and simulation of rotary shaft seals comprises a complex, coupled fluid-structure interaction problem with a number of submodels on multiple scales. There are various approaches available for this purpose. For instance, (Stakenborg, 1988; Stakenborg et al., 1990) investigated the radial deformation and contact pressure distribution based on ideal two-dimensional models of rotary shaft seals applying finite element analysis (FEA). (Wenk et al., 2016; Grün et al., 2021a, 2021b) extended this approach to three-dimensional models and investigated the contact behavior of rotary shaft seals in FEA considering measured surface data. EHL simulations were generally used to investigate the flow in the sealing gap of rotary shaft seals. A review of theoretical aspects especially with respect to EHL modeling can be found in (Salant, 2010). For this purpose, especially the Reynolds equations are evaluated, whereby the inertia and volume forces are neglected. For the analysis of micro structured sealing lips, (Keller et al., 2020) evaluated the complete Navier-Stokes equations in CFD. Furthermore, there is a lack of studies of the lubricant flow in the sealing gap of rotary shaft seals using CFD.

This paper presents an approach to simulate the lubricant flow in the sealing gap of rotary shaft seals applying CFD. The sealing edge geometry initially deformed during mounting and operation and the sealing gap height serve as input for the modeling. The deformed sealing edge geometry can be determined by FEA following (Grün et al., 2021a, 2021b). Analytical EHL

film thickness equations summarized in (Wheeler et al., 2016; Marian et al., 2020) provide an estimate of the sealing gap height and thus the radial deformation of the sealing edge surface at different operating points.

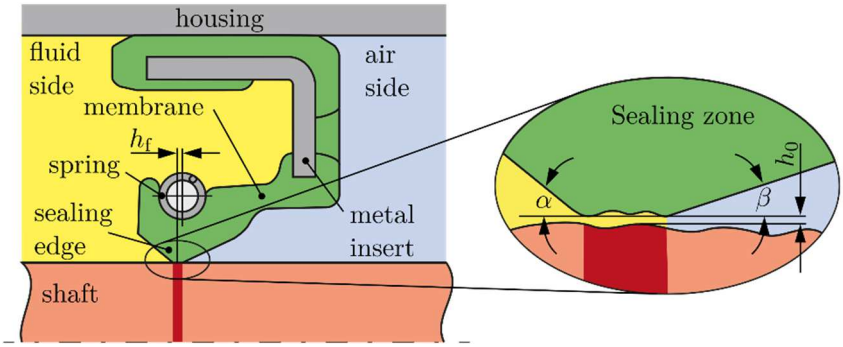

Fig. 1 – Elastomer sealing ring in the sealing system rotary shaft seal.

Computational Domain

A decisive step in modeling and simulation of the flow in the sealing gap is the definition of the computational domain. In the present study, FE simulations provide the input for the subsequent CFD analyses. A detailed description of the FE modeling and simulation of rotary shaft seals is given in (Grün et al., 2021a, 2021b). In this approach, a segment of the sealing ring is considered. After mounting on the shaft and applying the spring load, the shaft starts to rotate, distorting the sealing edge surface. Figure 2 illustrates the modeling process in this study. In addition to the deformed sealing edge surface, the previous FEA provides the structural mechanical normal force F. Together with the minimum gap height h_0, this yields the fluid domain for the subsequent discretization.

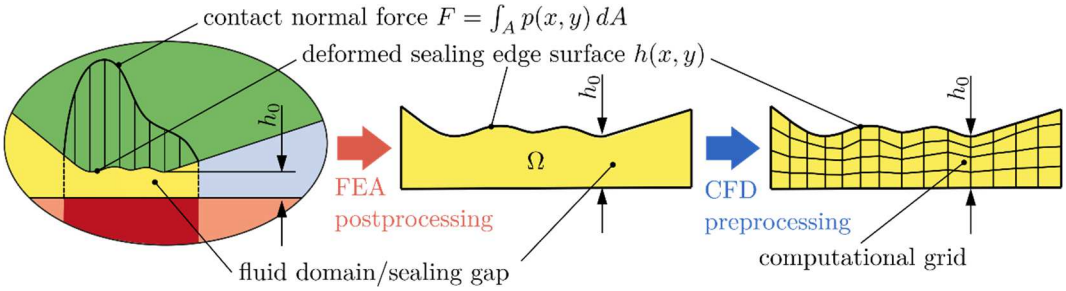

Fig. 2 – Principle process of modeling.

Figure 3 summarizes the FE modeling and visualizes the FEA results. In contrast to (Grün et al., 2021a, 2021b), the present study considers a synthetic sealing edge roughness similar to the approach of (Wennehorst and Poll, 2017). (Wang and Schipper, 2020) adopt a similar approach to approximate roughnesses. The surface roughness can be described via

$$z(x,y) = \Delta_x \sin\left(\frac{2\,\pi\,x}{\lambda_x}\right) + \Delta_y \sin\left(\frac{2\,\pi\,y}{\lambda_y}\right) \tag{1}$$

where λ_x and λ_y are the effective wavelength in circumferential direction x and in axial direction y. According to (Griffiths, 2001), the effective wavelengths are given by

$$\lambda_{x,y} = 2\,\pi\,\frac{S_q}{\sigma_{x,y}}, \tag{2}$$

where σ_x is the root mean square slope in the circumferential direction x and σ_y is the root mean square slope in the axial direction y. S_q is the root mean square roughness of the sealing edge surface. The amplitudes can be determined according to (Baglin, 1986) via

$$\Delta_x = \Delta_y = \sqrt{2}\, S_\mathrm{q}. \tag{3}$$

Roughness measurements on sealing edge surface similar to (Grün et al., 2021b) yield a root mean square roughness of $S_\mathrm{q} = 1.66\,\mu\mathrm{m}$ and a root mean square roughness slope in circumferential x and axial y direction of $\sigma_x = 87.8°$ and $\sigma_x = 89.7°$ as input data for surface roughness modeling.

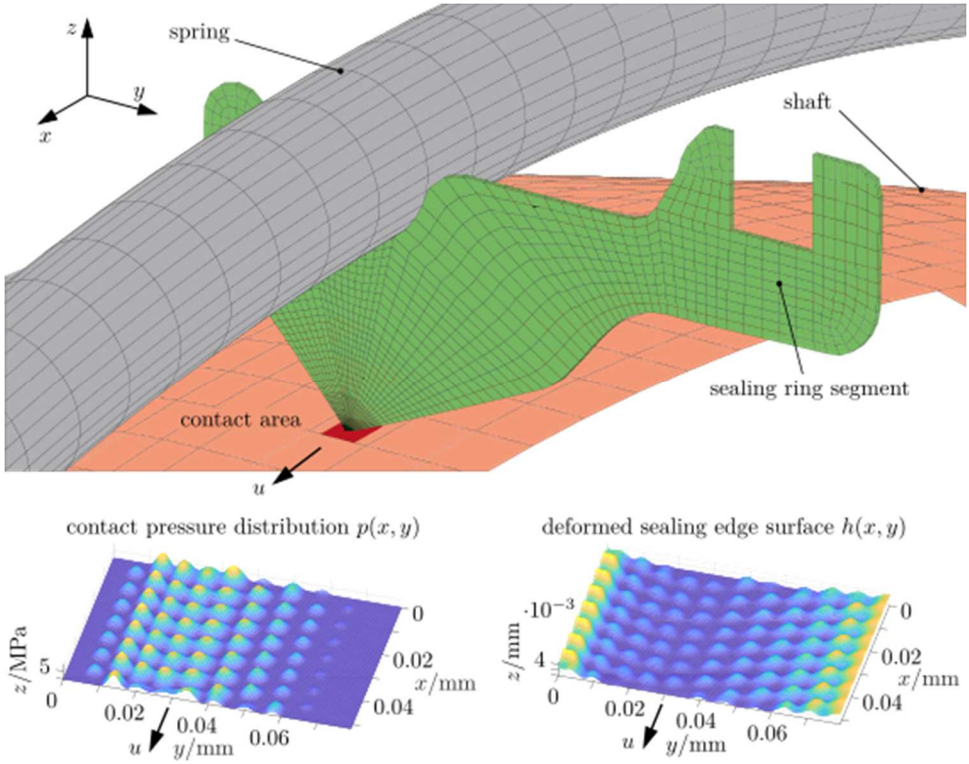

Fig. 3 – Illustration of the FE modeling and simulation.

After modeling and solving the structural mechanics of the rotary shaft seal, the inputs required for CFD can be determined in FE post-processing. These include the coordinates of the surface nodes $h(x,y)$ of the deformed sealing edge surface and the values for the contact pressure $p(x,y)$ at the corresponding nodes in the contact area. Starting from the shaft surface, all surface nodes of the sealing edge are exported with the pressure data up to a height of $h(x,y) \leq 5\ \mu\mathrm{m}$. The computational domain considered in the CFD, thus results as:

$$h_\mathrm{CFD}(x,y) = h(x,y) + h_0, \tag{4}$$

where h_0 is the minimum gap height respectively the lubricant film thickness. Analytical EHL equations serve to estimate the gap height h_0 in this study.

Material Properties

The lubricant data and the material parameters are essential for determining the sealing gap height via film thickness equations and for the definition of the fluid in CFD. Operating parameters such as temperature significantly affect the lubricant in the sealing gap of rotary shaft seals. (Feldmeth et al., 2016) presented a method for estimating the contact temperature

of rotary shaft seals. This allows the temperature in the sealing gap to be estimated for given operating conditions, friction conditions, fluid data and process-related settings.

The pressure-viscosity coefficient α_p and the dynamic viscosity η are considered temperature-dependent in the following. In the experimental studies to validate the numerical results, an additive-free mineral oil (FVA 3 reference oil, ISO VG 100) specified in (Forschungsvereinigung Antriebstechnik e. V., 1985) is used. The dynamic viscosity can be described as a function of temperature via

$$\eta(\vartheta) = \eta_{50}\, e^{B\frac{50°C-\vartheta}{C+\vartheta}+\alpha\, p}, \tag{5}$$

according to (Forschungsvereinigung Antriebstechnik e. V., 1985), whereby

$$\alpha = A_0 - A_1\,\vartheta + A_2\,\vartheta^2. \tag{6}$$

The temperature dependence of the pressure-viscosity coefficient is given by

$$\alpha_p(\vartheta) = -0.555\ln(\vartheta) + 4.0095, \tag{6}$$

which results from curve fitting based on the data sheet values from (Forschungsvereinigung Antriebstechnik e. V., 1985). Figure 4 and Figure 5 show the temperature dependence of the dynamic viscosity η and the pressure viscosity coefficient α_p.

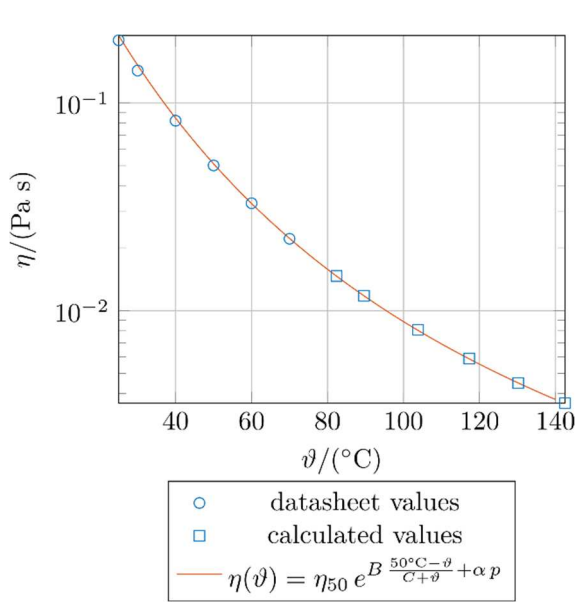

Fig. 4 – Dynamic viscosity vs. temperature.

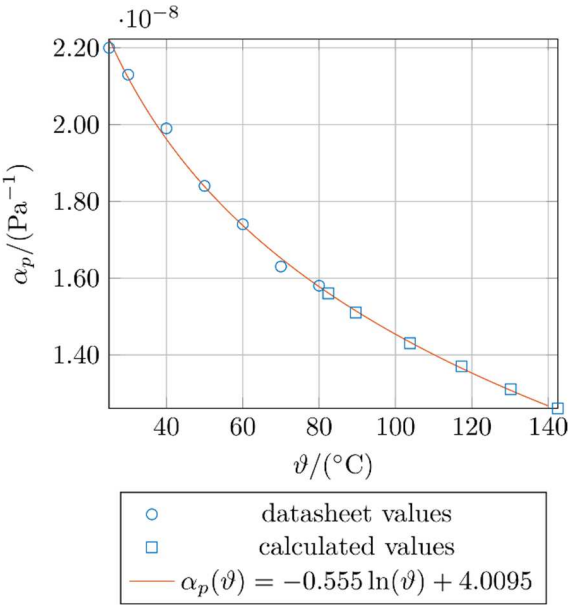

Fig. 5 – Pressure viscosity coefficient vs. temperature.

In the numerical analyses in this study, the rotary shaft seal is numerically investigated at six operating points. The lubricant temperature in the oil sump is $\vartheta_{\mathrm{sump}} = 80\ °\mathrm{C}$. The shaft has a diameter of $d = 80\ \mathrm{mm}$.

Table Table1 lists the applied lubricant data at the considered operating points. The contact temperature ϑ_{con} is estimated from (Feldmeth et al., 2016). Based on the contact temperature, the dynamic viscosity η and the pressure viscosity coefficients α_p in the sealing gap can be calculated via equations (5) – (7).

Table 1 – Lubricant parameters at different operating conditions.

rotational speed $n/(\mathrm{min}^{-1})$	circumferential velocity $u/(\mathrm{m\ s}^{-1})$	contact temperature $\vartheta_{\mathrm{con}}/(°\mathrm{C})$	dynamic viscosity $\eta/(\mathrm{Pa\ s})$	pressure viscosity coefficient $\alpha_p/(\mathrm{Pa}^{-1})$
500	2.1	82.4	0.0147	$1.56 \cdot 10^{-8}$
1000	4.2	89.6	0.0118	$1.51 \cdot 10^{-8}$
2000	8.4	103.8	0.0081	$1.43 \cdot 10^{-8}$
3000	12.6	117.3	0.0059	$1.37 \cdot 10^{-8}$
4000	16.8	130.2	0.0044	$1.31 \cdot 10^{-8}$
5000	20.9	142.5	0.0036	$1.26 \cdot 10^{-8}$

Film Thickness Equations

In the present study, six different analytical expressions provide the basis for estimating the sealing gap height. The gap height h_0 assumed in the following is the central lubricant film thickness h_c. For this purpose, (Dowson and Higginson, 1960; Dowson et al., 1962) introduced the material parameter

$$G = \alpha_p\, E', \tag{8}$$

the velocity parameter

$$U = \frac{\eta\, \dot{x}}{E' R_x}, \tag{9}$$

and the load parameter

$$W = \frac{F}{E'\, R_x^2}, \tag{10}$$

with the pressure-viscosity coefficient α_p, the dynamic viscosity η and the hydrodynamic effective velocity $\dot{x}$. The normal load F results from the pressure distribution after mounting shown in Figure 3. The reduced Young's modulus is given by

$$\frac{1}{E'} = \frac{1}{2}\left(\frac{1-\nu_1^2}{E_1} + \frac{1-\nu_2^2}{E_2}\right). \tag{11}$$

The radii of curvature in circumferential direction x and axial direction y result according to (Karami et al., 1987) via

$$R_{x,y} = \frac{1}{\sqrt{2}\, S_\mathrm{q}}\left(\frac{\lambda_{x,y}}{2\,\pi}\right). \tag{12}$$

Based on experimental results obtained by tribological tests and numerical results, (Hamrock and Dowson, 1977) determined the central lubricant film thickness

$$\frac{h_\mathrm{c}}{R_x} = 2.69\, U^{0.67}\, G^{0.53}\, W^{-0.067}\left(1 - 0.61\, e^{-0.75\left(\frac{R_x}{R_y}\right)^{0.64}}\right). \tag{13}$$

For low elastic moduli (Hamrock and Dowson, 1978) modified the equation to

$$\frac{h_\mathrm{c}}{R_x} = 7.32\, U^{0.64}\, W^{-0.22}\left(1 - 0.72\, e^{-0.28\left(\frac{R_x}{R_y}\right)}\right). \tag{14}$$

Based on the parameters given in (8) - (10), (Moes, 1965) introduced the modified load parameter

$$M = W\,(2\,U)^{\frac{3}{4}}, \tag{15}$$

and the viscosity parameter

$$L = G\,(2\,U)^{\frac{1}{4}}. \tag{16}$$

(Evans and Snidle, 1981) took this up and suggested the analytical expression for central lubricant film thickness

$$\frac{h_\mathrm{c}}{R_x(2\,U)^{0.5}} = 1.7\, M^{-0.026}\, L^{0.40}. \tag{17}$$

(Chittenden et al., 1985) extended previous approaches and introduced the central lubricant film thickness

$$\frac{h_c}{R_x} = 4.31\, U^{0.68}\, G^{0.49}\, W^{-0.073} \left(1 - e^{-1.23\left(\frac{R_y}{R_x}\right)^{\frac{2}{3}}}\right). \tag{18}$$

(Nijenbanning et al., 1994) applied a multilevel solver to estimate the central lubricant film thickness

$$\frac{h_c}{R_x (2\,U)^{0.5}} = \left(\left(H_{RI}^{\frac{3}{2}} + (H_{EI}^{-4} + H_{00}^{-4})^{-\frac{3}{8}}\right)^{\frac{2\,s}{3}} + (H_{EI}^{-8} + H_{00}^{-8})^{-\frac{s}{8}}\right)^{\frac{1}{s}} \tag{19}$$

by curve fitting. They distinguished the asymptotic regimes rigid isoviscous

$$H_{RI} = 145 \left(1 + 0.796\, D^{\frac{14}{15}}\right)^{-\frac{15}{7}} D^{-1}\, M^{-2}, \tag{20}$$

elastic isoviscous

$$H_{EI} = 3.18 \left(1 + 0.006\, \ln(D) + 0.63\, D^{\frac{4}{7}}\right)^{-\frac{14}{15}} D^{-\frac{1}{15}}\, M^{-\frac{2}{15}}, \tag{21}$$

rigid piezoviscous

$$H_{RP} = 1.29\, (1 + 0.691\, D)^{-\frac{2}{3}}\, L^{\frac{2}{3}}, \tag{22}$$

and elastic piezoviscous

$$H_{EP} = 1.48 \left(1 + 0.006\, \ln(D) + 0.63\, D^{\frac{4}{7}}\right)^{-\frac{7}{20}} D^{-\frac{1}{24}}\, M^{-\frac{1}{12}}\, L^{\frac{3}{4}}, \tag{23}$$

where

$$D = \frac{R_x}{R_y} \tag{24}$$

is the ratio of the reduced radii of curvature and the parameters

$$s = 1.5 \left(1 + e^{-1.2\frac{H_{EI}}{H_{RI}}}\right) \tag{25}$$

and

$$H_{00} = 1.8\, D^{-1} \tag{26}$$

ensure a smooth transition between the asymptotic solutions.

(Masjedi and Khonsari, 2015) solved the modified Reynolds equation, the surface deformation and elasto-plastic asperity contact equations simultaneously to analyze the film thickness and asperity load ratio. Based on curve fitting to the results, the central lubricant film thickness is given by

$$\frac{h_c}{R_x} = 3.672\, U^{0.663\, k^{0.025}}\, G^{0.502\, k^{0.064}}\, W^{-0.045\, k^{0.18}}\, (1 - 0.573\, e^{-0.74\, k}). \tag{27}$$

Figure 6 shows the calculated lubricant film thicknesses and gap heights at the defined operating points using the models presented. The lubricant data from

Table 1 and the structural parameters from Table 2 serve as input data. The structural parameters are assumed to be independent of temperature. The equations according to (Chittenden et al., 1985; Nijenbanning et al., 1994; Masjedi and Khonsari, 2015) provide comparable lubricant film thicknesses. (Evans and Snidle, 1981) yields comparatively high and (Hamrock and Dowson, 1977) the lowest lubricant film thicknesses

.

Table 2 – Structural parameters.

Young's modulus of the seal	E_1	$8.04 \cdot 10^6$	Pa
Poisson's ratio of the seal	ν_1	0.5	–
Young's modulus of the shaft	E_2	$210 \cdot 10^6$	Pa
Poisson's ratio of the shaft	ν_2	0.3	–
root mean square roughness (sealing edge surface)	S_q	$1.66 \cdot 10^{-6}$	m
root mean square roughness slope in circumferential direction x	σ_x	1.53	–
root mean square roughness slope in axial direction y	σ_y	1.56	–
effective wavelength in circumferential direction x	λ_x	$6.81 \cdot 10^{-6}$	m
effective wavelength in axial direction y	λ_y	$6.66 \cdot 10^{-6}$	m
radius of curvature in circumferential direction x	R_x	$0.50 \cdot 10^{-6}$	m
radius of curvature in circumferential direction y	R_y	$0.48 \cdot 10^{-6}$	m
normal force (0.1°-segment)	F	0.0054	N

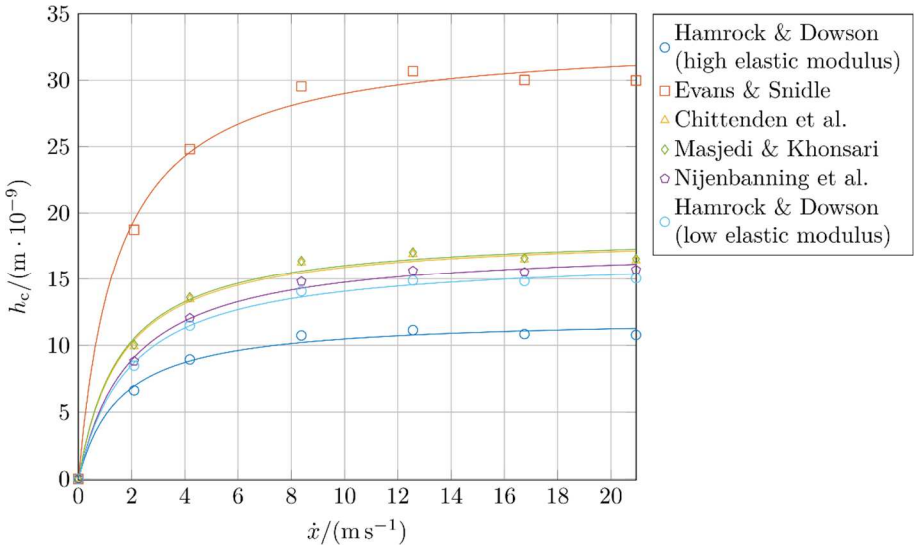

Fig. 6 – Lubricant film thickness vs. speed.

Meshing

A Script serves for automatic discretization of the lubricant film in the sealing gap. It generates a structured computational grid consisting of hexahedral cells. The principle flow of the script is shown in Figure 7. The main function addresses various subroutines during the run. The input for the meshing algorithm consists of an initial surface, described by node coordinates and the sealing gap height h_0. The three $n_x \times n_y$ matrices $\boldsymbol{X}, \boldsymbol{Y}$ and $\boldsymbol{Z}$ define the surface coordinates. Based on the input of the sample points in x and y direction n_x and n_y, the initial surface mesh is interpolated (*refineMesh.m*). The number of nodes in z direction is defined by the number of cell layers n_z.

The function *getNodes.m* is used to set up the node matrix $\boldsymbol{N}^{n_x \cdot n_y \cdot (n_z+1) \times 3}$ containing all node coordinates of the computational grid. Input data are the three interpolated surface coordinate matrices $\boldsymbol{X}, \boldsymbol{Y}$ and $\boldsymbol{Z}$ and the number of cell layers n_z in z direction. The node matrix is constructed in three nested loops as shown in Algorithm 1. Each loop represents one dimension. Starting from the origin, a row of node coordinates in the x direction is determined in the inner loop. At the end of each row, the y coordinate of the next row is determined in the middle loop

and the inner loop are executed again. Once the coordinates of one layer are determined, the index is increased in the outer loop and the next layer is built up again by the middle and inner loops.

Based on the node matrix $\boldsymbol{N}$, the algorithm constructs the hexahedral cells of the computational grid and declares the respective quadrilateral cell faces according to the node indices. Figure 8 illustrates the node numbering of a single grid cell and the adjacency between the cells, defined by the cell faces. Three functions serve to declare the topology of the computational grid. One sets up the cell matrix $\boldsymbol{C}$. Two others declare the inner and outer cell faces $\boldsymbol{F}_{\mathrm{int}}$ and $\boldsymbol{F}_{\mathrm{ext}}$ including adjacency relationships.

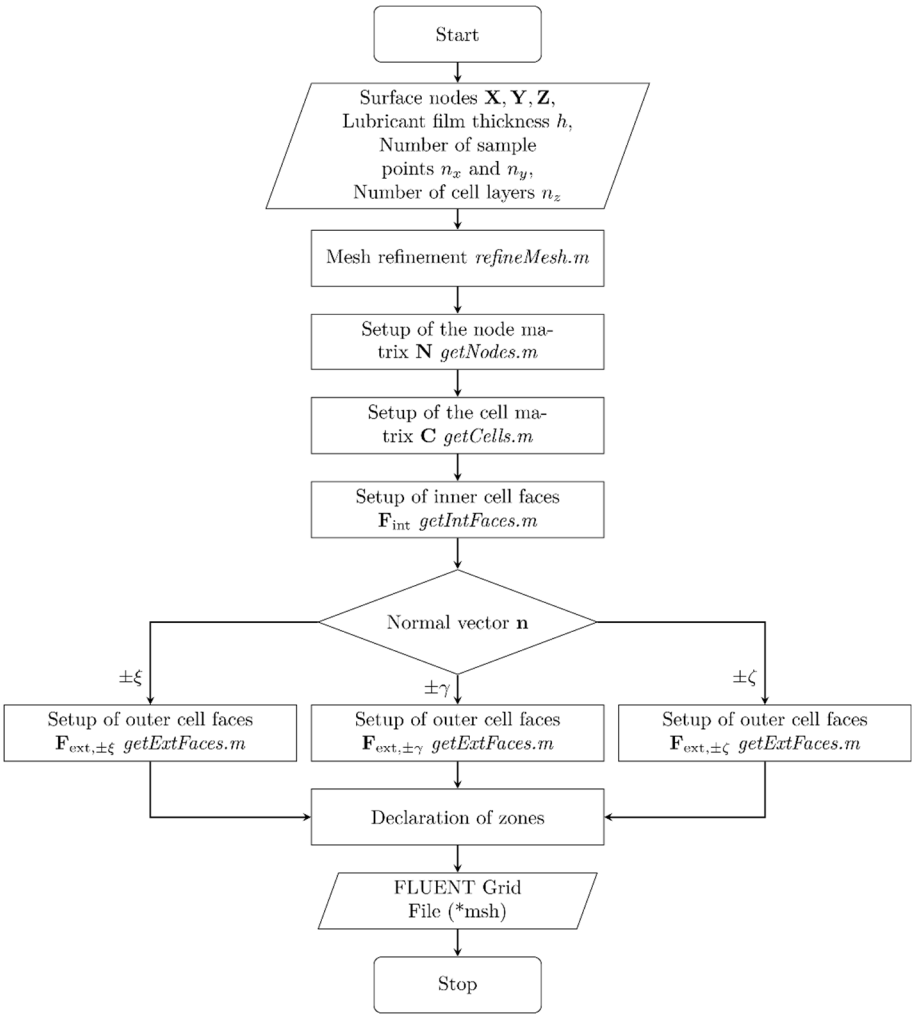

Fig. 7 – Flow chart of automated meshing.

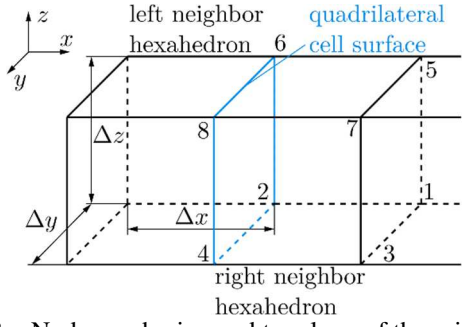

Fig. 8 – Node numbering and topology of the grid cell.

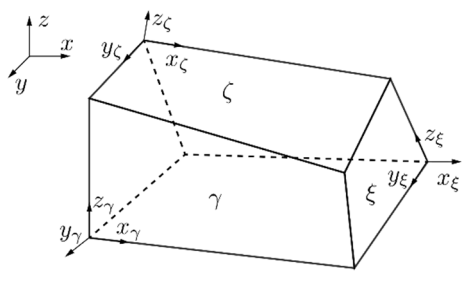

Fig. 9 – Face declaration of a general hexahedron.

Algorithm 1: ***getNodes.m***

Input: $\mathbf{X}, \mathbf{Y}, \mathbf{Z}, \mathrm{n_z}$
Output: $\mathbf{N}$
/* Initialization */
$\mathrm{i} = 1$
/* Setup of the node matrix */
for $\mathrm{k} = \mathrm{n_z}: -1: 0$ /* Loop over layers */
  for $\mathrm{n} = \mathrm{n_y}: -1: 1$ /* Loop over y coordinates */
    for $\mathrm{m} = \mathrm{n_x}: -1: 1$ /* Loop over x coordinates */
      /* Node coordinates */
      $\mathrm{x} = \mathbf{X}(\mathrm{m}, \mathrm{n})$
      $\mathrm{y} = \mathbf{Y}(\mathrm{m}, \mathrm{n})$
      $\mathrm{z} = \mathbf{Z}(\mathrm{m}, \mathrm{n}) \cdot (1 - 1/\mathrm{n_z})$
      $\mathbf{N}(\mathrm{i}, :) = [\mathrm{x} \quad \mathrm{y} \quad \mathrm{z}]$
      $\mathrm{i} = \mathrm{i} + 1$
    end for
  end for
end for

The function *getCells.m* links the nodes to hexahedral cells and thereby determines the respective cell nodes. The input parameters are n_x, n_y and n_z. Starting from the origin, Algorithm 2 assembles the cells first in x direction, then in y direction and finally in z direction in three nested loops. Output data is the cell matrix $\boldsymbol{C}^{n_c \times 8}$, where n_c is the number of cells in the computational domain.

Algorithm 2: ***getCells.m***

Input: $\mathrm{n_x}, \mathrm{n_y} \mathrm{n_z}$
Output: $\mathbf{C}, \mathrm{n_c}$
/* Initialization */
$\mathrm{i} = 1$
$\mathrm{n_c} = (\mathrm{n_x} - 1)(\mathrm{n_y} - 1)\mathrm{n_z}$
/* Setup of the cell matrix */
for $\mathrm{k} = 0: (\mathrm{n_z} - 1)$
  for $\mathrm{n} = 1: (\mathrm{n_y} - 1)$
    for $\mathrm{m} = 1: (\mathrm{n_x} - 1)$
      /* Cell nodes */
      $\mathrm{nd_{i,1}} = \mathrm{n} + (\mathrm{m} - 1) \cdot \mathrm{n_x} + \mathrm{k} \cdot \mathrm{n_z}$
      $\mathrm{nd_{i,2}} = \mathrm{nd_{i,1}} + 1$
      $\mathrm{nd_{i,3}} = \mathrm{n} + \mathrm{m} \cdot \mathrm{n_x} + \mathrm{k} \cdot \mathrm{n_z}$
      $\mathrm{nd_{i,4}} = \mathrm{nd_{i,3}} + 1$
      $\mathrm{nd_{i,5}} = \mathrm{nd_{i,1}} + \mathrm{n_z}$
      $\mathrm{nd_{i,6}} = \mathrm{nd_{i,2}} + \mathrm{n_z}$
      $\mathrm{nd_{i,7}} = \mathrm{nd_{i,3}} + \mathrm{n_z}$
      $\mathrm{nd_{i,8}} = \mathrm{nd_{i,4}} + \mathrm{n_z}$
      $\mathbf{C}(\mathrm{i}, :) = [\mathrm{nd_{i,1}} \quad \mathrm{nd_{i,2}} \quad \mathrm{nd_{i,3}} \quad \mathrm{nd_{i,4}} \quad \mathrm{nd_{i,5}} \quad \mathrm{nd_{i,6}} \quad \mathrm{nd_{i,7}} \quad \mathrm{nd_{i,8}}]$
      $\mathrm{i} = \mathrm{i} + 1$
    end for
  end for
end for

As shown in Figure 8, each quadrilateral cell face has at least one adjacent cell. The adjacency definition is based on the Cartesian law system. The right adjacent cell c_r is relatively located in the respective positive axis direction and the left c_l in the negative one. A distinction is made between inner and outer cell faces. While the inner cell faces are located within the fluid domain and have one right and one left adjacent hexahedron each, the outer cell faces have only one

left or one right adjacent cell, depending on their location. Furthermore, the outer cell surfaces serve to define the necessary boundary conditions for the simulation. Normal vectors describe the orientation of the cell faces in local coordinate systems. For this purpose, Figure 9 introduces the face declaration. The maximum component of the normal vector on the respective plane defines the face designation. This means that the face with maximum x component is denoted by ξ. Analogously, the normal vectors with maximum y and z components result in the faces γ and ζ.

The function *getIntFaces.m* aims to determine the inner cell faces of the computational grid with the two respective adjacent cells. The input is the cell matrix $\boldsymbol{C}$, the number of cells n_c and the number of nodes n_x, n_y and n_z in x, y and z direction. Algorithm 3 shows the setup of the inner cell faces ξ . The inner cell faces γ and ζ can be determined analogously. For this purpose, the loop structure shown is repeated for each of the other two spatial directions. In each run of the inner loop, the corresponding face nodes are extracted from the cell matrix $\boldsymbol{C}$. As shown in Figure 8, the cell nodes $2, 4, 6,$ and 8 constitute the cell face ξ_j of cell j. The right adjacent cell $c_{\mathrm{i,r}}$ corresponds to the current cell j and the left adjacent cell $c_{\mathrm{i,l}}$ to the previous cell $j-1$. The result is the matrix $F^{n_\mathrm{int}\times 6}$, containing the n_int inner cell faces with their respective adjacent cells $c_{\mathrm{i,r}}$ and $c_{\mathrm{i,l}}$.

Algorithm 3: *getIntFaces.m*

Input: $\mathbf{C}, \mathrm{n_c}, \mathrm{n_x}, \mathrm{n_y}\ \mathrm{n_z}$
Output: $\mathbf{F}_\mathrm{int}, \mathrm{n_{int}}$
/* Initialization */
$\mathrm{i} = 1$
$\mathrm{j} = 1$
$\mathrm{n_{int}} = \mathrm{n_c}/\mathrm{n_z}(\mathrm{n_z}-1)\left((\mathrm{n_x}-2)(\mathrm{n_y}-1)+(\mathrm{n_y}-2)(\mathrm{n_x}-1)\right)\mathrm{n_z}$
/* Setup of the inner cell faces */
for $\mathrm{k} = 1{:}\,\mathrm{n_z}$
  for $\mathrm{n} = 1{:}\,\mathrm{n_c}/\mathrm{n_z}$
    for $\mathrm{m} = 1{:}\,\mathrm{n_c}/\mathrm{n_z} - 1$
      /* Face declaration */
      $\mathrm{F} = \mathrm{C(j,[2\quad 4\quad 8\quad 6]}$
      $\mathrm{c_l} = \mathrm{j}$ /* Left neighbor */
      $\mathrm{c_r} = \mathrm{j}+1$ /* Right neighbor */
      $\mathbf{F}_\mathrm{int}(\mathrm{i},:) = [\mathrm{F}\quad \mathrm{c_r}\quad \mathrm{c_l}]$
      $\mathrm{i} = \mathrm{i}+1$
      $\mathrm{j} = \mathrm{j}+1$
    end for
    $\mathrm{j} = \mathrm{j}+1$
  end for
  $\mathrm{j} = \mathrm{n_z}\cdot\mathrm{k}+1$
end for

The function *getExtFaces.m* serves to specify the outer cell faces of the hexahedrons at the borders of the computational domain. The main script transfers the cell matrix $\boldsymbol{C}$, the total number of cells n_c, the number of cell layers n_z and the number of nodes n_x, n_y and n_z in x, y and z direction to the subroutine shown in Algorithm 4. The function performs a case distinction to determine the position of the outer boundary faces. The orientation of the normal vector $\boldsymbol{n}$ is passed for this purpose. Algorithm 4 considers the outer cell faces with normal vector $+\boldsymbol{n}_\xi$. The outer cell faces at the remaining boundaries of the computational domain are determined analogously. Only the initialization of the indexing of the cells and the cell faces differs. Algorithm 4 determines the face nodes of cell face ξ_j and the two adjacent cells c_r and c_l. As the normal vector $+\boldsymbol{n}_\xi$ is oriented positively and is located on a cell face at the border of the

computational grid, there is no right adjacent cell. Therefore, the right adjacent c_r is assigned a 0. Output parameters is the outer cell face matrix $\boldsymbol{F}_{\mathrm{ext},+\xi}$.

Algorithm 4: ***getExtFaces.m***

```
Input: C, n_c, n_z, ±n
Output: F_ext
switch(±n)
    case(+n_ξ)
        /* Initialization
        i = 1
        j = n_x − 1
        for k = 1: n_z
            for m = 1: n_y − 1
                F = C(j, [2  4  8  6])
                c_l = j                          /* Left neighbor */
                c_r = 0                          ./* Right neighbor */
                F_ext(i, :) = [F  c_r  c_l]
                i = i + 1
                j = j + (n_x − 1)
            end for
            j = n_c/n_z · k + (n_x − 1)
        end for
    end case
    case(−n_ξ)
    …
    end case
…
end switch
```

After the subroutines set up the matrices describing the grid topology of the computational domain, the main script writes the matrices to a FLUENT grid file (*msh). This file format has the advantage that it can be imported into many common CFD applications. A detailed description of the structure of the file format can be found in (ANSYS, 2021). Figure 10 shows the discretized computational domain of the lubricant film in the sealing gap of a rotary shaft seal.

Boundary conditions

The pre-processing and solving of the computational domain is performed with ANSYS CFX 19.1. For this purpose, the generated FLUENT grid file is imported into CFX. The material definition depends on the temperature and consequently on the circumferential speed. The lubricant data for the operating conditions considered are listed in Table 1.

The boundary cell faces on the air and fluid sides are defined as boundary conditions "openings". This boundary condition type is appropriate when the complete description at this position is not known in advance. For example, the pressure at the corresponding position is known, but the direction of the flow is not. The top boundary cell faces correspond to the interface to the solid sealing edge surface and the bottom to the interface to the solid shaft surface. Hence, they are defined as "walls". This boundary condition type represents an impermeable boundary for the fluid flow. The bottom wall (shaft surface) is subjected to the circumferential velocity $\dot{x}$. The top wall (sealing edge surface) is stationary. The considered computational domain represents a segment of the lubricant film, analogous to the structural simulations in Figure 3. Consequently, the boundary cell faces are coupled in circumferential direction via a translational periodic interface.

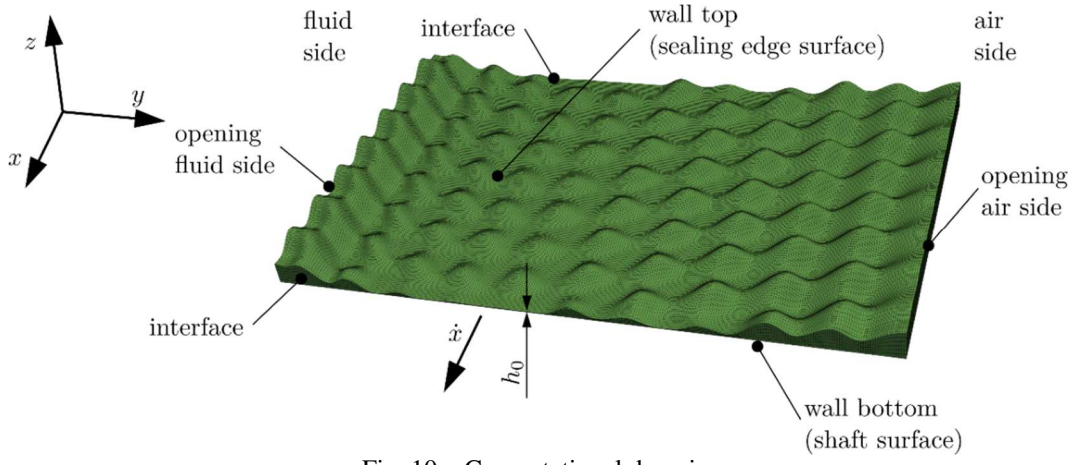

Fig. 10 – Computational domain.

RESULTS

The plausibility of the simulation results is checked by comparison with experimental results. For this purpose, the two sealing characteristics pumping rate $\dot{m}$ and friction torque T have become established (Bauer, 2021a. In the numerical analyses, the sealing edge surface is rough and the shaft surface is ideally smooth. In order to satisfy this assumption in the test rig experiments as accurately as possible and to be able to achieve comparable results, polished shafts provide the sealing counterfaces. The shafts employed have an arithmetic mean deviation of the roughness profile $R_\mathrm{a} = 0.00649 \ldots 0.0163\ \mu\mathrm{m}$, a maximum height of the roughness profile $R_\mathrm{z} = 0.0876 \ldots 0.248\ \mu\mathrm{m}$ and a maximum peak-to-valley height of the sampling lengths on the roughness profile $R_\mathrm{max} = 0.142 \ldots 0.322\ \mu\mathrm{m}$.

The pumping rate is measured experimentally as described in (Kawahara and Hirabayashi, 1979). The sealing ring is mounted inversely so that fluid is constantly available on the actual air side and can be pumped through the sealing gap. The difference between the mass flow over the cell faces on the fluid side and the mass flow over the cell faces on the air side results in the pumping rate in the simulated lubricant film segment. The computed total pumping rate of the rotary shaft seal results from the extrapolation to the circumference of the shaft. Figure 11 compares the computed pumping rates with the measured pumping rates. The presented pumping rates of each experiment result from the mean value over five measured values. The pumping rates for the different lubricant film thickness equations differ only slightly. The computated pumping rates are lower than the measured pumping rates. The calculated as well as the measured pumping rates show a linear dependency over the circumferential velocity. Thus, the presented model qualitatively approximates the correlation between circumferential speed and pumping rate, but quantitatively shows differences. One reason for the differences between measurement results and numerical results is that the polished shaft surface is quite smooth but does not correspond to the model idea of an ideally smooth surface. This leads to different hydrodynamics in the lubricant film and can affect the pumping rate.

The friction torque is determined in additional experiments according to (Schulz et al., 2018). The friction torque in the lubricant film segment is obtained by multiplying the simulated tangential force in the segment under consideration and the shaft radius. The calculated friction torque of the rotary shaft seal results from the extrapolation to the shaft circumference. Figure 12 shows the measured and calculated friction torques versus circumferential speed. Similar to the pumping rates, there are only marginal differences in the friction torques for the different lubricant film thicknesses. The friction torque from the experimental tests is higher than the calculated torque. The friction torque curves are fitted based on rational models. The computed

friction torque converges to a constant value after a rapid increase. The rational model used has a numerator and a denominator polynomial of the first degree. The friction torque measurements also show an initial rapid increase followed by a slight decrease in the friction torque over the circumferential velocity. The curve fitting employs a rational model with a first-degree numerator polynomialand a second-degree denominator polynomial. This allows a better approximation of the decrease in the friction torque at higher circumferential speeds. Despite the quantitative differences, the numerical model qualitatively shows the same physical behavior. The lubrication modes provide an explanation for the quantitative differences. While the CFD model applied here only considers the case of full-film lubrication, mixed and boundary lubrication can also occur in the experimental tests. This increases the friction. Another reason for the differences is that the present model does not consider the churning torque in the fluid chamber. As described in (Feldmeth et al., 2013), this can have a significant influence on the measured friction torque.

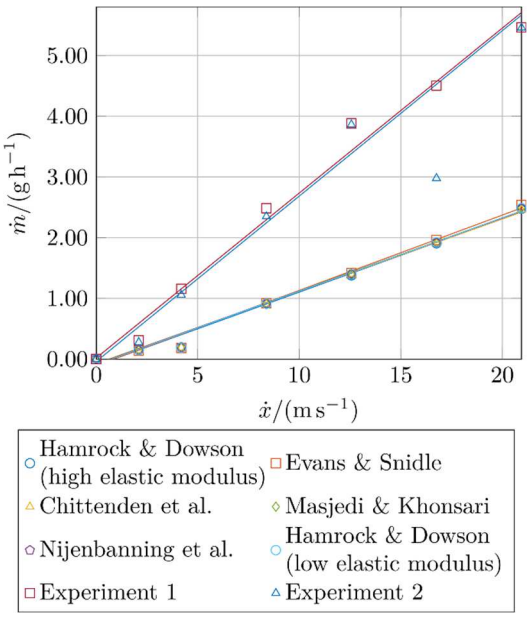

Fig. 11 – Pumping rate vs. circumferential velocity.

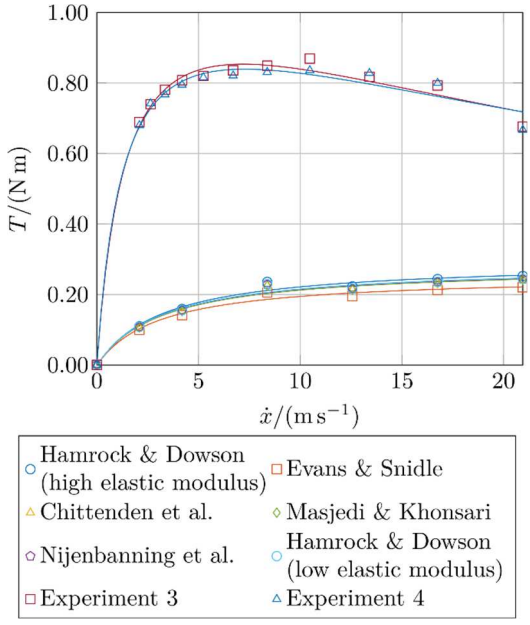

Fig. 12 – Friction torque vs. circumferential velocity.

In summary, although the model provides quantitatively different values, it can qualitatively describe the operating behavior of rotary shaft seals. The main benefit of the computed results is that they provide an insight into the microscopic flow processes in the sealing gap of rotary shaft seals. Figure 13 shows the pressure distribution in the lubricant film in the sealing gap. Here, the sealing gap height is $h_0 \cong 30$ nm based on the film thickness equation given in (17) at $\dot{x} \cong 12.6\,\mathrm{m\,s^{-1}}$. The hydrodynamic pressure has an asymmetric pressure distribution in axial y direction. The maximum pressure is oriented to the fluid side. Pressure peaks arise in the areas in front of the compressed asperities of the sealing edge surface, where the minimum gap height is located. In the valleys of the roughness, the pressure decreases significantly. These pressure differences cause vortices in the flow in the lubricant film, as shown in Figure 14. In the areas where the sealing gap height is comparatively high, the streamlines are oriented in the circumferential direction and the velocity corresponds to the relative velocity between the sealing edge and shaft surface. At the points with the minimum sealing gap heights and the pressure peaks, the fluid is retarded, vortexed and thus axially deflected. This effect causes the active back-pumping mechanism of rotary shaft seals in operation, according to (Kammüller, 1986; Müller, 1987).

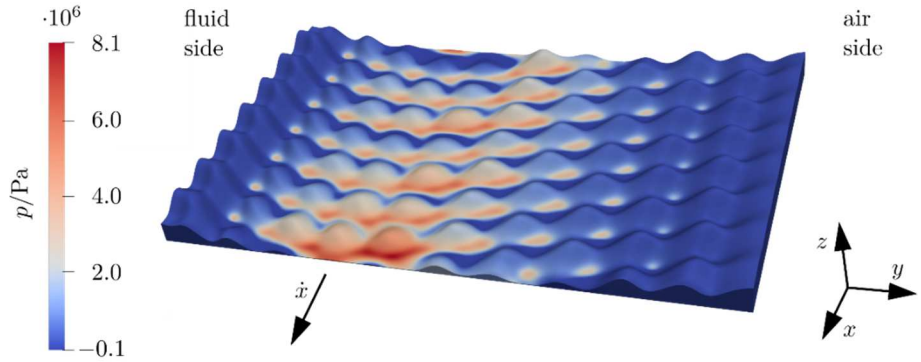

Fig. 13 – Pressure distribution in the sealing gap.

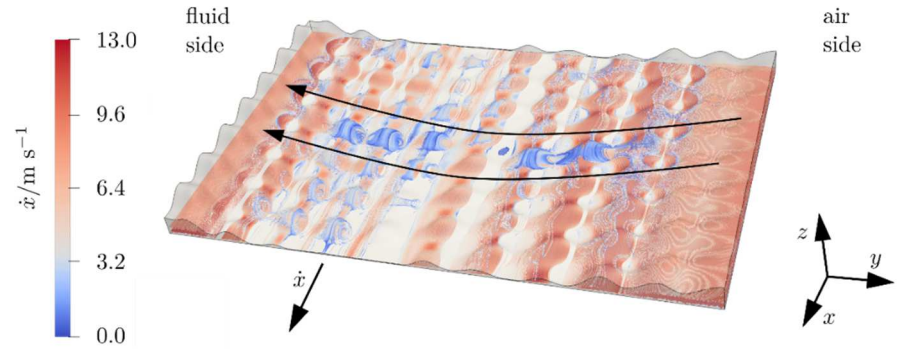

Fig. 14 – Lubricant flow in the sealing gap.

CONCLUSIONS

This paper deals with Computational Fluid Dynamics (CFD) of the fluid domain respectively the lubricant film in the sealing gap of rotary shaft seals. The deformed sealing edge surface and the pressure distribution after mounting obtained from Finite Element Analysis (FEA) serve as input for the modeling of the lubricant film. A script is presented which automatically discretizes lubricant films with different geometries based on an initial surface and the minimum gap height. The minimum gap height is estimated via established lubricant film thickness equations. The lubricant data required as input is estimated for the different circumferential speeds. The discretization and the generation of the computational grid are described in detail. Experimental results are compared with the numerical results and discussed on the basis of the sealing parameters pumping rate and friction torque. The numerical model qualitatively shows the same physical behavior as the real sealing system, but underestimates the pumping rate and the friction torque. Nevertheless, the Computational Fluid Dynamics (CFD) provide plausible results as well as a comprehensive understanding of the lubricant flow in the sealing gap of rotary shaft seals. In addition, it serves as the basis for a simple and fast study of a wide variety of tribological effects, such as contact temperature or different lubricants.

REFERENCES

[1] ANSYS, I. (2021) Ansys® Fluent, Release 2019 R1, Help System, Fluent User's Guide.

[2] Baglin, K.P. (1986) Elastohydrodynamic Pressure Rippling in Cylinders Finished with a Circumferential Lay, Proceedings of the Institution of Mechanical Engineers, Part C: Journal of Mechanical Engineering Science, 200(5), pp.335–347.

[3] Bauer, F. (2021a) Federvorgespannte-Elastomer-Radial-Wellendichtungen. Wiesbaden: Springer Fachmedien Wiesbaden.

[4] Bauer, F. (2021b) Tribologie. Wiesbaden: Springer Fachmedien Wiesbaden.

[5] Chittenden, R.J. et al. (1985) A theoretical analysis of the isothermal elastohydrodynamic lubrication of concentrated contacts. II. General case, with lubricant entrainment along either principal axis of the Hertzian contact ellipse or at some intermediate angle, Proceedings of the Royal Society of London. A. Mathematical and Physical Sciences, 397(1813), pp.271–294.

[6] Dowson, D. and Higginson, G.R. (1960) The Effect of Material Properties on the Lubrication of Elastic Rollers, Journal of Mechanical Engineering Science, 2(3), pp. 188–194.

[7] Dowson, D., Higginson, G.R. and Whitaker, A. V. (1962) Elasto-Hydrodynamic Lubrication: A Survey of Isothermal Solutions, J. Mech. Eng. Science, 4(2), pp. 121–126.

[8] Evans, H.P. and Snidle, R.W. (1981) The isothermal elastohydrodynamic lubrication of spheres, Journal of Tribology, 103(4), pp.547–557.

[9] Feldmeth, S., Bauer, F. and Haas, W. (2013) Einfluss des Planschmoments bei der Reibungsmessung am Dichtsystem Radial-Wellendichtung, in 54. Tribologie-Fachtagung. Göttingen: Gesellschaft für Tribologie e.V., pp.86/1-86/11.

[10] Feldmeth, S.,et al. (2016) Abschätzung der Kontakttemperatur bei Radial-Wellendichtungen mit der selbstentwickelten Open-Source-Software InsECT, in KISSsoft AG (Hg.) 2016 – Tagungsband Schweizer Maschinenelemente Kolloquium SMK, pp.233–248.

[11] Forschungsvereinigung Antriebstechnik e. V. (1985) Referenzöle für Wälz- und Gleitlager-, Zahnrad- und Kupplungsversuche.

[12] Griffiths, B. (2001) Manufacturing Surface Technology. 1st edn. Elsevier.

[13] Grün, J., Feldmeth, S. and Bauer, F. (2021a) The sealing mechanism of radial lip seals: A numerical study of the tangential distortion of the sealing edge, in Vencl, A. (ed.) 10th International Conference on Tribology – BALKANTRIB ’20 PROCEEDINGS. Belgrade, pp.165–166.

[14] Grün, J., Feldmeth, S. and Bauer, F. (2021b) Wear on radial lip seals: a numerical study of the influence on the sealing mechanism, Wear, 476, pp.203674.

[15] Hamrock, B.J. and Dowson, D. (1977) Isothermal Elastohydrodynamic Lubrication of Point Contacts: Part III—Fully Flooded Results, Journal of Lubrication Technology, 99(2), pp.264–275.

[16] Hamrock, B.J. and Dowson, D. (1978) Elastohydrodynamic Lubrication of Elliptical Contacts for Materials of Low Elastic Modulus I—Fully Flooded Conjunction, Journal of Lubrication Technology, 100(2), pp.236–245.

[17] Kammüller, M. (1986) Zur Abdichtwirkung von Radial-Wellendichtringen. Universität Stuttgart.

[18] Karami, G., Evans, H.P. and Snidle, R.W. (1987) Elastohydrodynamic Lubrication of Circumferentially Finished Rollers having Sinusoidal Roughness, Proceedings of the Institution of Mechanical Engineers, Part C: J. of Mechanical Engineering Science, 201(1), pp.29–36.

[19] Kawahara, Y. and Hirabayashi, H. (1979) A Study of Sealing Phenomena on Oil Seals, A S L E Transactions, 22(1), pp.46–55.

[20] Keller, D., Jacobs, G. and Neumann, S. (2020) Development of a Low-Friction Radial Shaft Seal: Using CFD Simulations to Optimise the Microstructured Sealing Lip, Lubricants, 8(4), p.41.

[21] Marian, M. et al. (2020) Non-Dimensional Groups, Film Thickness Equations and Correction Factors for Elastohydrodynamic Lubrication: A Review, Lubricants, 8(10), p.95.

[22] Masjedi, M. and Khonsari, M.M. (2015) On the effect of surface roughness in point-contact EHL: Formulas for film thickness and asperity load, Tribology International, 82(PA), pp.228–244.

[23] Moes, H. (1965) Communications, in Symposium on Elastohydrodynamic Lubrication. London, pp.244–245.

[24] Müller, H.K. (1987) Concepts of sealing mechanism of rubber lip type rotary shaft seals., in 11th International Conference on Fluid Sealing. Cannes, pp.698–709.

[25] Nijenbanning, G., Venner, C.H. and Moes, H. (1994) Film thickness in elastohydrodynamically lubricated elliptic contacts, Wear, 176(2), pp.217–229.

[26] Salant, R.F. (2010) Soft elastohydrodynamic analysis of rotary lip seals, Proceedings of the Institution of Mechanical Engineers, Part C: Journal of Mechanical Engineering Science, 224(12), pp.2637–2647.

[27] Schulz, M. et al. (2018) Influence of different shaft surface finishes on the tribological and functional behaviour of radial shaft seals, in Silva Gomes, J.F. and Meguid, S.A. (eds) 7th International Conference Integrity-Reliability-Failure. Funchal, pp.351–368. Available at: https://paginas.fe.up.pt/~irf/Proceedings_IRF2020/.

[28] Stakenborg, M.J.L. (1988) On the sealing mechanism of radial lip seals, Tribology International, 21(6), pp.335–340.

[29] Stakenborg, M.J.L., van Leeuwen, H.J. and ten Hagen, E.A.M. (1990) Visco-Elastohydrodynamic (VEHD) Lubrication in Radial Lip Seals: Part 1—Steady-State Dynamic Viscoelastic Seal Behavior, Journal of Tribology, 112(4), pp.578–583.

[30] Wang, C. and Schipper, D.J. (2020) A numerical-analytical approach to determining the real contact area of rough surface contact, Tribology - Materials, Surfaces & Interfaces, 14(3), pp.166–176.

[31] Wenk, J.F. et al. (2016) A multi-scale finite element contact model using measured surface roughness for a radial lip seal, Tribology International [Preprint].

[32] Wennehorst, B. and Poll, G. (2017) Soft micro-elastohydrodynamic lubrication and friction at rough conformal contacts, Proceedings of the Institution of Mechanical Engineers, Part J: Journal of Engineering Tribology, 231(3), pp.302–315.

[33] Wheeler, J.-D. et al. (2016) On the relevance of analytical film thickness EHD equations for isothermal point contacts: Qualitative or quantitative predictions?, Friction, 4(4), pp.369–379.